J. Fluid Mech. (2023), *vol*. 975, A27, doi:10.1017/jfm.2023.860

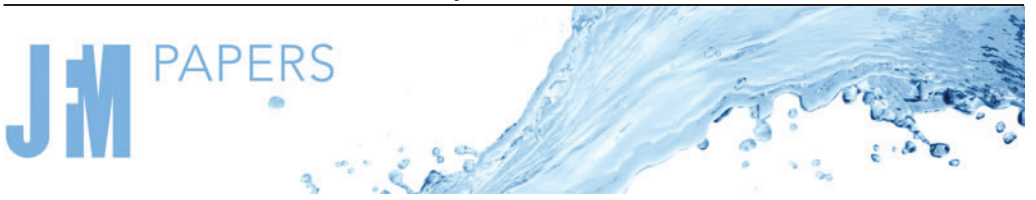

The mean wall-normal velocity in turbulent boundary layer flows under pressure gradient

Tie Wei[1],†, Zhaorui Li[2], Tobias Knopp[3] and Ricardo Vinuesa[4]

[1]Department of Mechanical Engineering, New Mexico Tech, Socorro, NM 87801, USA

[2]Department of Engineering, Texas A&M University-Corpus Christi, Corpus Christi, TX 78412, USA

[3]Institute of Aerodynamics and Flow Technology, DLR (German Aerospace Center), Bunsenstr. 10, 37073 Gottingen, Germany

[4]FLOW, Engineering Mechanics, KTH Royal Institute of Technology, Stockholm, Sweden

(Received 24 April 2023; revised 9 October 2023; accepted 10 October 2023)

Using a combination of proper variable transformation and integral methods, we rigorously derive an analytical formulation for the mean wall-normal velocity in turbulent boundary layers (TBLs) subjected to arbitrary pressure gradients. The accuracy and robustness of this novel formulation are validated extensively through comparisons with two independent sets of numerical simulation data, demonstrating excellent agreement in both near-equilibrium and non-equilibrium TBLs. In addition, the robustness of the analytical formulations to various choices of boundary-layer edge definition is further confirmed in non-equilibrium TBLs. Our formulation includes a streamwise derivative term, which has minimal significance in near-equilibrium TBLs but plays a crucial role in determining the mean wall-normal velocity in non-equilibrium TBLs. Moreover, we investigate the physical significance of the pre-factors associated with the mean wall-normal velocity components, and unveil a close connection between a previously defined pressure gradient parameter and the ratio of these pre-factors in the analytical equation governing the mean wall-normal velocity. The insights gained from the examination of the pre-factors and their connection to the pressure gradient parameter offer valuable knowledge for interpreting and predicting the behaviour of turbulent boundary layers in various practical applications.

Key words: boundary layer structure

† Email address for correspondence: tie.wei@nmt.edu

1. Introduction

Turbulent boundary layers (TBLs) play a crucial role in the design and operation of a wide range of practical systems, including aircraft, ships, wind turbines and other fluid systems. A key aspect of understanding TBLs is their behaviour under pressure gradients, as this significantly impacts the performance and energy efficiency of these systems. For instance, under an adverse pressure gradient (APG), the flow within the TBL slows down, and the thickness of the boundary layer increases. In severe cases of APG, the boundary-layer flow may separate from the solid surface, resulting in a drastic change in the flow pattern.

Considerable research efforts have been dedicated to understanding the behaviour of TBLs under pressure gradients through theoretical, experimental and numerical means (Rotta 1950; Clauser 1954; Townsend 1956; Mellor 1966; Mellor & Gibson 1966; Monty, Harun & Marusic 2011; Bobke *et al.* 2017; Coleman, Rumsey & Spalart 2018; Devenport & Lowe 2022; Subrahmanyam, Cantwell & Alonso 2022). However, previous investigations have concentrated primarily on studying the effects of pressure gradients on the mean streamwise velocity, with relatively less attention given to the behaviour of the mean wall-normal flow. This knowledge gap motivates our present study, where we rigorously derive a novel analytical equation for the mean wall-normal velocity in TBLs subjected to arbitrary pressure gradients.

Experimental measurement of the mean wall-normal velocity V poses significant challenges due to its small magnitude relative to the streamwise velocity. As a result, there is a scarcity of reliable experimental data available for studying V. To overcome this limitation and ensure the validity of the derived analytical equation, this study conducts a comprehensive comparison with two independent numerical simulation datasets. The first dataset consists of well-resolved large-eddy simulations (LES) of near-equilibrium APG TBLs conducted by Bobke *et al.* (2017). The second dataset comprises direct numerical simulations (DNS) of TBLs subjected to first an APG and then a favourable pressure gradient (FPG) (Coleman *et al.* 2018).

An important challenge in the study of TBLs (particularly when subjected to streamwise pressure gradients) is to determine accurately and consistently the boundary-layer edge (see e.g. Vinuesa *et al.* 2016; Cantwell 2021; Griffin, Fu & Moin 2021). The conventional approach relies on mean streamwise velocity (U) profiles and locates the boundary-layer edge at 99 % of the free-stream velocity (see e.g. Young *et al.* 2007). However, this method assumes a constant mean streamwise velocity outside the boundary layer, which may not always hold true (see Appendix A for examples). To address this, we adopt a novel method proposed by Wei & Knopp (2023) to determine the boundary-layer edge (δ_e). This method identifies the boundary-layer edge as the location where the Reynolds shear stress decreases to 1 % of its maximum value. Further details about this method can be found in Appendix A. This new approach aligns with the traditional boundary-layer edge determination method when the mean streamwise velocity remains constant outside the boundary layer. The analytical derivation developed in this work is independent of the specific choice of δ_e and U_e. In the main text, the results utilize the δ_e determined using the new approach. Additionally, in Appendix B, the results obtained using δ_e defined from the U profiles and diagnostic plot (Vinuesa *et al.* 2016) are presented for comparison.

Figure 1 illustrates the variation of the mean streamwise velocity at the boundary-layer edge U_e for the two simulations examined in this study. In the well-resolved near-equilibrium flat-plate LES by Bobke *et al.* (2017), the pressure gradient was imposed through specifying the free-stream velocity at the top of the domain using Townsend's power-law definition (see Townsend 1956; Mellor & Gibson 1966) $C(x - x_0)^m$, where C is a constant, x_0 is a virtual origin, and m is the power-law exponent. Five cases

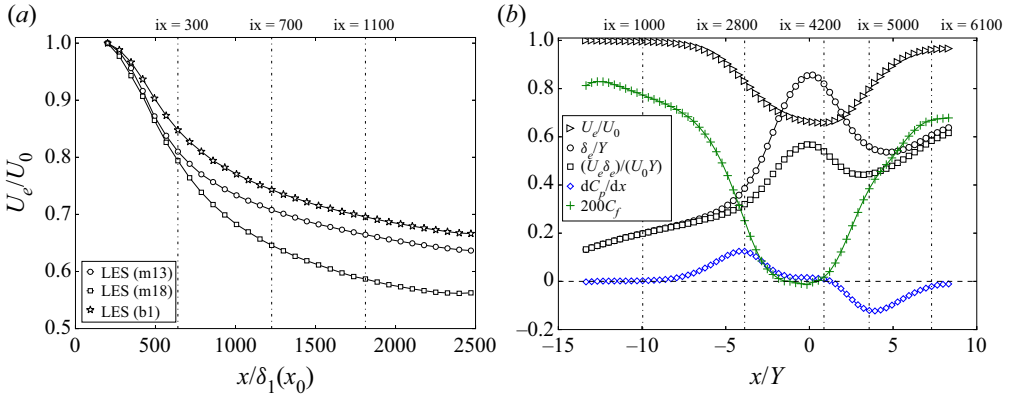

Figure 1. Variation of the mean streamwise velocity at the boundary-layer edge. The ix on the top axis refers to the grid-point number in the x-direction. (a) Well-resolved LES of near-equilibrium flat-plate APG TBLs by Bobke *et al.* (2017). The x-location is normalized by the displacement thickness of the laminar inflow $\delta_1(x_0)$. (b) DNS of NEPG TBLs by Coleman *et al.* (2018). The x-location is normalized by the simulation domain height Y.

of simulations were performed to investigate different near-equilibrium boundary layers by varying the virtual origin and the power-law exponent m. These simulations include case m13 ($x_0 = 60$, $m = -0.13$), case m16 ($x_0 = 60$, $m = -0.16$), case m18 ($x_0 = 60$, $m = -0.18$), case b1 ($x_0 = 100$, $m = -0.14$), and case b2 ($x_0 = 100$, $m = -0.18$). The lengths in the archived data were normalized by the displacement thickness of the laminar inflow $\delta_1(x_0)$, and the velocities were normalized by the free-stream velocity at the inlet U_0.

In the DNS of non-equilibrium pressure gradient (NEPG) TBLs by Coleman *et al.* (2018), pressure gradients were induced by a transpiration profile $V_{top}(x)$ acting through a virtual parallel plane offset a fixed distance Y from the flat no-slip surface. The archived simulation data were normalized by Y and $U_0 = U_e(x_0)$. Figure 1(b) illustrates that the boundary-layer thickness increases much more rapidly under APG than under zero pressure gradient (ZPG). Although U_e decreases under APG, the product $U_e\delta_e$ increases in the x-direction. The maximum value of $U_e\delta_e$ in the APG region is reached near ix $\approx$ 4000. Based on the friction coefficient $C_f = \tau_{wall}/(0.5\rho U_e^2)$ data, the TBL separates at $x/Y \approx -1.4$ (ix $\approx$ 3500) and subsequently reattaches at $x/Y \approx 0.4$ (ix $\approx$ 4050). Based on the pressure gradient dC_p/dx data presented in figure 1(b), it can be determined that the FPG region initiates at approximately ix = 4200. The pressure coefficient C_p is defined as $C_p = (P - P_\infty)/(0.5\rho U_\infty^2)$.

Figure 1(b) shows that under FPG, initially δ_e decreases in the x-direction. However, between ix $\approx$ 5200 and ix $\approx$ 6000, the boundary-layer thickness δ_e increases again, despite the mean pressure gradient being favourable. Similarly, the product $U_e\delta_e$ initially decreases in the FPG region, but then increases again in the x-direction. It is important to note that due to the sudden transition from APG to FPG, the FPG region in the DNS may be influenced by the upstream APG effect, especially in the outer region.

Figure 2 displays the variation of the mean wall-normal velocity at several x-stations in the numerical simulations. Under APG, the mean wall-normal velocity is positive and increases linearly outside the boundary layer. On the other hand, under FPG (as seen in the DNS at ix = 5000), the mean wall-normal velocity is negative, and the boundary-layer thickness decreases in the x-direction. Figure 2(b) shows that the mean wall-normal

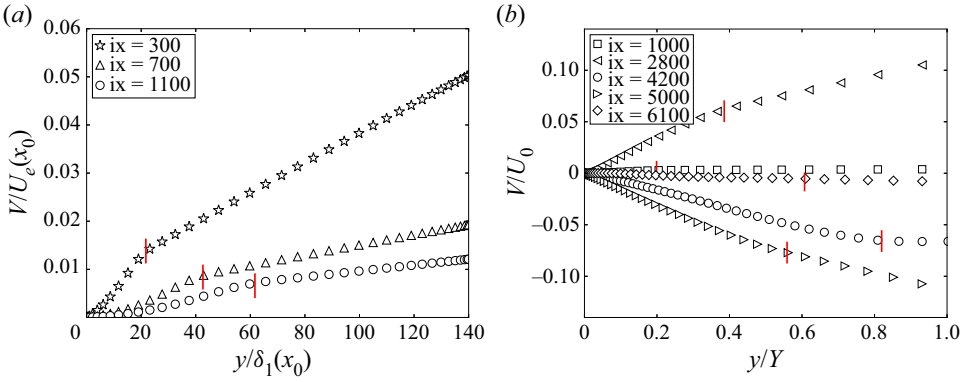

Figure 2. Mean wall-normal velocity profiles at different x-locations shown in figure 1. (*a*) Well-resolved LES of near-equilibrium flat-plate APG TBLs by Bobke *et al.* (2017) (case b1). (*b*) The DNS of NEPG TBLs by Coleman *et al.* (2018). The short vertical red line marks the boundary-layer edge.

velocity at or near ZPG (ix = 1000 and 6100) is significantly smaller than the mean wall-normal velocity under APG.

In this work, we elucidate the characteristics of the wall-normal velocity through an analytical derivation. In § 2, the mean wall-normal velocity at the boundary-layer edge is first derived. An analytical equation for the mean wall-normal velocity is subsequently derived and validated with the numerical simulation data. Section 3 discusses the significance of the components and pre-factors in the analytical equation. Section 4 summarizes the work.

2. Analysis of the mean continuity equation

For a statistically steady two-dimensional TBL under pressure gradient, the mean continuity equation is (see e.g. Tennekes & Lumley 1972)

$$0 = \frac{\partial U}{\partial x} + \frac{\partial V}{\partial y}, \tag{2.1}$$

where the upper-case letters U and V represent the mean velocity component in the streamwise (x) and wall-normal (y) directions, respectively. In order to derive an analytical equation for the mean wall-normal velocity V, we first transform the mean continuity equation into a dimensionless form. To achieve this, we define the normalized variables

$$x^* \overset{\text{def}}{=} \frac{x}{L}, \quad y^- \overset{\text{def}}{=} \frac{y}{\delta_e(x)}, \quad U^-(x^*, y^-) \overset{\text{def}}{=} \frac{U_e(x) - U(x,y)}{U_e(x)}, \quad V^-(x^*, y^-) \overset{\text{def}}{=} \frac{V(x,y)}{|V_e(x)|}, \tag{2.2a–d}$$

where L is a length scale in the x-direction. While normalized streamwise velocity can also be U/U_e, in this work, we define U^- as $1 - U/U_e$ for a bounded integral $\int_0^\infty U^- \,\mathrm{d}y^-$. It is important to emphasize that this normalization does not assume any self-similarity of U^- or V^-.

Using the defined normalized variables, the terms in the mean continuity equation can be written as

$$\left.\begin{aligned}\frac{\partial U}{\partial x} &= \frac{\mathrm{d}U_e}{\mathrm{d}x} - \frac{\mathrm{d}U_e}{\mathrm{d}x}U^- - \frac{U_e}{L}\frac{\partial U^-}{\partial x^*} + \frac{U_e}{\delta_e}\frac{\mathrm{d}\delta_e}{\mathrm{d}x}y^- \frac{\partial U^-}{\partial y^-},\\ \frac{\partial V}{\partial y} &= \frac{|V_e|}{\delta_e}\frac{\partial V^-}{\partial y^-}.\end{aligned}\right\} \tag{2.3}$$

Simple mathematics produces a dimensionless continuity equation in the form

$$0 = \frac{\delta_e}{|V_e|}\frac{\mathrm{d}U_e}{\mathrm{d}x} - \frac{1}{|V_e|}\frac{\mathrm{d}(U_e\delta_e)}{\mathrm{d}x}U^- + \frac{U_e}{|V_e|}\frac{\mathrm{d}\delta_e}{\mathrm{d}x}\frac{\partial(y^-U^-)}{\partial y^-} - \frac{U_e}{|V_e|}\frac{\delta_e}{L}\frac{\partial U^-}{\partial x^*} + \frac{\partial V^-}{\partial y^-}. \tag{2.4}$$

2.1. *Mean wall-normal velocity at the boundary-layer edge*

The mean wall-normal velocity V_e at the edge of the boundary layer can be obtained by performing integration of (2.4) with respect to y^- from the wall $y^- = 0$ to the boundary-layer edge $y^- = 1$:

$$V_e = -\delta_e\frac{\mathrm{d}U_e}{\mathrm{d}x} + \frac{\mathrm{d}(U_e\delta_e)}{\mathrm{d}x}\frac{\delta_1}{\delta_e} + U_e\frac{\delta_e}{L}\int_0^1 \frac{\partial U^-}{\partial x^*}\,\mathrm{d}y^-. \tag{2.5}$$

Note that by definition, $\int_0^1 U^-\,\mathrm{d}y^- = \delta_1/\delta_e$, where δ_1 is the mass displacement thickness (see Schlichting 1979). In a ZPG TBL, the mean streamwise velocity beyond the boundary-layer edge δ_e remains constant in the wall-normal y-direction. However, when a TBL is subjected to a pressure gradient, the mean streamwise velocity beyond δ_e may vary in the y-direction (see Appendix A). The evaluation of the last term in (2.5) involves absorbing the length scale L back into x^*. As a result, the specific choice of L becomes inconsequential to the evaluation.

Figure 3 illustrates the simulation data for V_e, accompanied by the three terms on the right-hand side of (2.5), as well as their sum. The simulation data exhibit excellent agreement with the analytical equation (2.5). In figure 3(*a*), it is evident that the term involving $\partial U^-/\partial x^*$ is relatively small within the near-equilibrium APG TBL ($1000 < x/\delta_1(x_0) < 2200$), and its contribution can be considered negligible in such situations. However, as shown in figure 3(*b*), the term involving $\partial U^-/\partial x^*$ becomes significant when the TBL undergoes rapid changes in pressure gradient, and cannot be neglected.

By applying the Leibniz integral rule to the last term in (2.5), the mean wall-normal velocity at the boundary-layer edge can be simplified as

$$V_e = -\delta_e\frac{\mathrm{d}U_e}{\mathrm{d}x} + \frac{\mathrm{d}(U_e\delta_1)}{\mathrm{d}x}. \tag{2.6}$$

For a ZPG boundary layer, where U_e remains constant, (2.6) can be simplified further to $V_e = U_e\,\mathrm{d}\delta_1/\mathrm{d}x$, as reported by Wei, Li & Wang (2023*a*).

It is intriguing to observe that the functional form of (2.6) exhibits certain similarities to Kármán's integral equation $u_\tau^2 = (U_e\delta_1)\,\mathrm{d}U_e/\mathrm{d}x + \mathrm{d}(U_e^2\delta_2)/\mathrm{d}x$. Kármán's integral equation is derived by integrating globally both the mean continuity and momentum equations (see e.g. Schlichting 1979). Equation (2.6) is also valid for the laminar (Falkner–Skan) case, as it is derived solely from the continuity equation without making any assumptions about turbulence or pressure gradients.

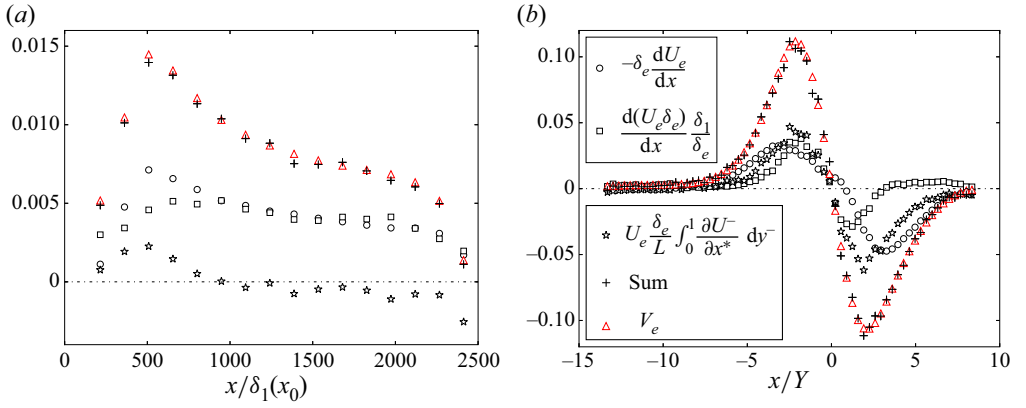

Figure 3. Comparison of simulation data of V_e with (2.5). (*a*) Case b1 from the LES of Bobke *et al.* (2017). (*b*) The DNS of Coleman *et al.* (2018). To prevent clutter, every 100th grid in the x-direction is plotted. Markers for V_e represent values obtained directly from simulation data, while the sum is calculated from terms on the right-hand side of (2.5).

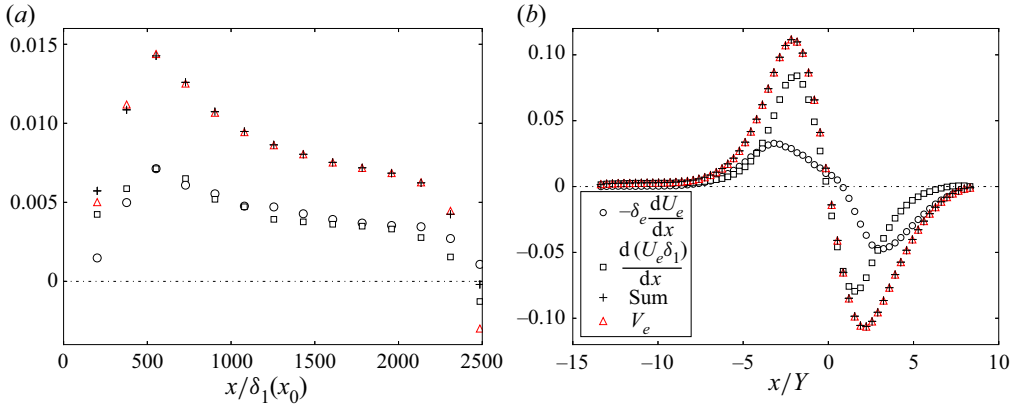

Figure 4. Comparison of simulation data of V_e with (2.6). (*a*) Case b1 from the LES of Bobke *et al.* (2017). (*b*) The DNS of Coleman *et al.* (2018). To prevent clutter, every 100th grid in the x-direction is plotted. Markers for V_e represent values obtained directly from simulation data, while the sum is calculated from terms on the right-hand side of (2.6).

Figure 4 illustrates the simulation data of V_e, along with the two terms on the right-hand side of (2.6), and their sum. The mean wall-normal velocity magnitude is observed to be significantly higher under APG or FPG as compared to ZPG. This amplified wall-normal convection in the APG TBL has been reported in simulations of TBLs around wing sections (Vinuesa *et al.* 2018). Figure 4 demonstrates that the sum of the terms on the right-hand side of (2.6) exhibits better agreement with the directly simulated V_e in comparison to the sum of the terms on the right-hand side of (2.5). Mathematically, (2.5) and (2.6) are equivalent. The enhanced accuracy observed in the post-processing with (2.6) can be attributed to its improved precision in calculating the x-derivative from δ_1, which represents an integral quantity. In Appendix B, we demonstrate that the validity of (2.6) is independent of the method used to determine the boundary-layer edge (see figure 18).

Figure 4 shows that in APG TBLs, both terms on the right-hand side of (2.6) are positive, and V_e is also positive, resulting in the rapid growth of the boundary layer.

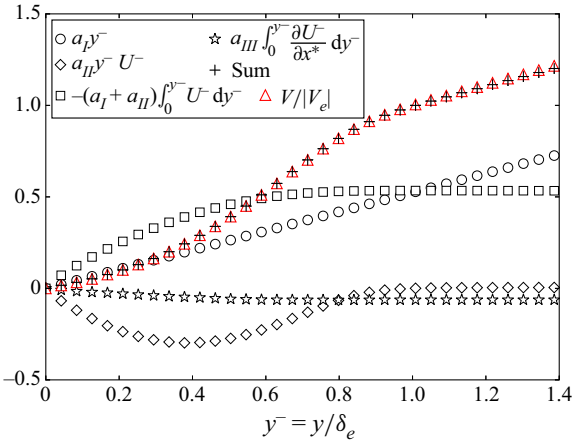

Figure 5. Illustration of the four components in (2.7) for an APG TBL. The data are from the well-resolved LES data of near-equilibrium APG TBLs by Bobke *et al.* (2017): case b1 at the 1000th grid point in x.

Conversely, under FPG, U_e increases in the x-direction, and as shown in figure 4(b), the first term on the right-hand side of (2.6) becomes negative.

2.2. *Analytical equation for V*

Integrating (2.4) with respect to y^- yields an analytical equation for the mean wall-normal velocity distribution:

$$V^- = \underbrace{-\frac{\delta_e}{|V_e|}\frac{\mathrm{d}U_e}{\mathrm{d}x}}_{a_I} y^- \underbrace{-\frac{U_e}{|V_e|}\frac{\mathrm{d}\delta_e}{\mathrm{d}x}}_{a_{II}} y^- U^- + \underbrace{\frac{1}{|V_e|}\frac{\mathrm{d}(U_e\delta_e)}{\mathrm{d}x}}_{-(a_I+a_{II})} \int_0^{y^-} U^- \,\mathrm{d}y^- + \underbrace{\frac{U_e}{|V_e|}\frac{\delta_e}{L}}_{a_{III}} \int_0^{y^-} \frac{\partial U^-}{\partial x^*} \,\mathrm{d}y^-. \tag{2.7}$$

For a constant value of U_e, (2.7) simplifies to $V^- = (U_e/|V_e|)\,\mathrm{d}\delta_e/\mathrm{d}x(-y^- U^- + \int_0^{y^-} U^-\,\mathrm{d}y^-) + (U_e/|V_e|)(\delta_e/L)\int_0^{y^-}(\partial U^-/\partial x^*)\,\mathrm{d}y^-$, as reported by Wei *et al.* (2023*a*) for the normalized mean wall-normal velocity in a ZPG boundary layer.

To illustrate the four components of the mean wall-normal velocity in an APG TBL, figure 5 uses the well-resolved LES data of near-equilibrium APG TBLs by Bobke *et al.* (2017). Under an APG, U_e experience a decrease while δ_e increases in the x-direction. As a result, a_I is positive and a_{II} is negative.

Figure 6 shows the different components of the mean wall-normal velocity under transition from APG to FPG, as obtained from the DNS of Coleman *et al.* (2018). In the APG section, the first, second and third terms in the DNS data behave similarly to those shown in figure 5. However, the last term with x-derivative has a significantly larger magnitude in the DNS data, indicating that the TBL is not in a near-equilibrium state. In the FPG section, the first and last terms of (2.7) are negative, as shown in figure 6(b).

To provide further validation of (2.7), the mean wall-normal velocity profiles at various x-stations presented in figure 2 are normalized and compared with the analytical equation

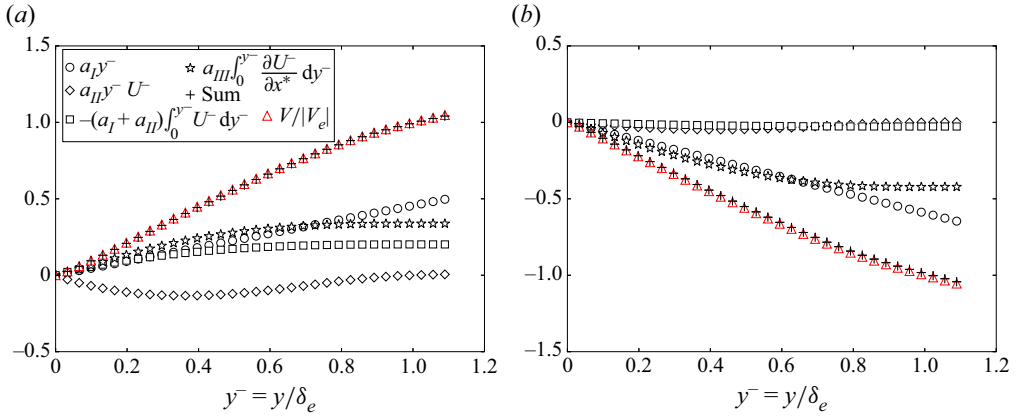

Figure 6. Wall-normal velocity and its components from the DNS data of NEPG TBLs by Coleman *et al.* (2018). (*a*) The APG section at ix = 2800. (*b*) The FPG section at ix = 5000.

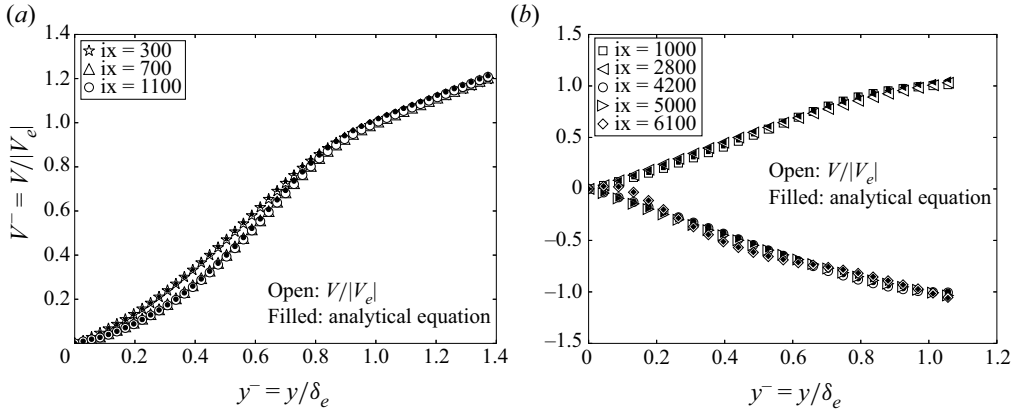

Figure 7. Normalized $V/|V_e|$ obtained directly from simulation data (open symbols) and the sum of terms on the right-hand side of (2.7) (filled symbols) plotted against y/δ_e. (*a*) Well-resolved LES data of near-equilibrium APG TBLs by Bobke *et al.* (2017). (*b*) The DNS data of NEPG TBLs by Coleman *et al.* (2018).

in figure 7. The figure demonstrates the excellent agreement between the simulation data and the analytical equation. In Appendix B, we demonstrate that the accuracy of (2.7) is not affected by the method used to determine the boundary-layer edge (see figure 20). The shapes of the $V/|V_e|$ versus y/δ_e profiles, however, may vary due to the use of different methods for determining the boundary-layer edge and the resulting differences in δ_e and V_e values (see Appendix B).

In ZPG TBL, V^- is approximately a self-similar function of y^-, as observed by Wei & Klewicki (2016). However, in TBL under pressure gradient, especially when the pressure gradient varies over a short distance, the mean wall-normal velocity profile undergoes a rapid change in shape and magnitude. Figure 8 presents the mean wall-normal velocity profiles around the location where the pressure gradient switches from APG to FPG. In figure 8(*a*), the raw data show a smaller magnitude of V (magnitude of 0.02 in figure 8(*a*) versus 0.1 in figure 2(*b*)), and a change of velocity direction. Moreover, the shapes of the mean wall-normal velocity at the three stations are distinctively different. In figure 8(*b*), the mean wall-normal velocity normalized by $|V_e|$ is presented.

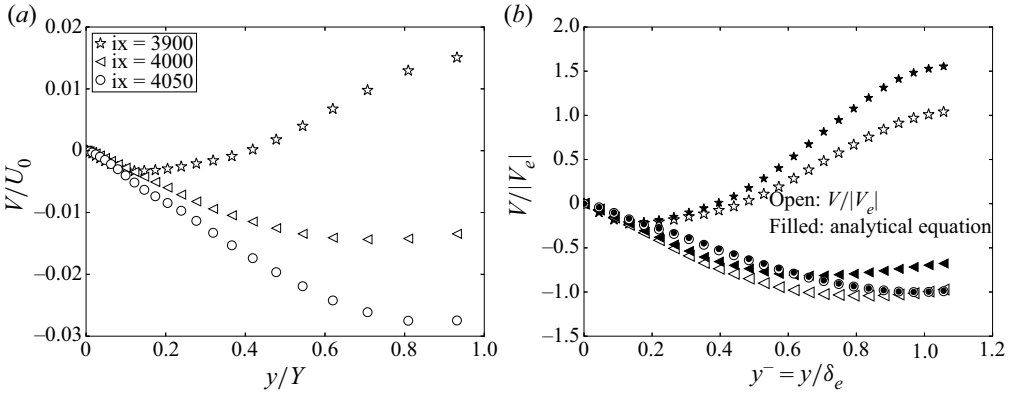

Figure 8. Plots of V profiles from DNS data of NEPG TBLs by Coleman *et al.* (2018) at three different locations near $x/Y = 0$: (*a*) raw data, (*b*) normalized data.

While the analytical equation captures the general trend of V, there are noticeable deviations at stations ix = 3900 and 4000. These deviations can be attributed to the rapid shift from APG to FPG, which amplifies the numerical errors in the finite-difference calculation of $\partial U^-/\partial x^*$ in (2.7) at ix = 3900 and 4000.

3. Discussion

The analytical equation (2.7) provides valuable insights into the composition of the mean wall-normal velocity in TBLs under arbitrary pressure gradients. It reveals that the mean wall-normal velocity can be decomposed into four distinct components, as depicted in figures 5 and 6. It is interesting to note that the first three components in (2.7) for the mean wall-normal velocity in the TBL bear a strong resemblance to those observed for the mean transverse flow in planar turbulent wakes under pressure gradients, as discussed in Wei *et al.* (2023*b*).

The parameters a_I, a_{II}, $-(a_I + a_{II})$ and a_{III} in (2.7) represent the ratios of the characteristic velocity for each component to $|V_e|$. Figure 9 illustrates the variations of these parameters with x-locations. In near-equilibrium APG TBLs, a_I is approximately 0.5, and a_{II} is negative with magnitude approximately 2. In the DNS of TBL under rapid changes between APG and FPG, a_I varies between -1 and 1. The magnitudes of a_{II} and $-(a_I + a_{II})$ are approximately 1, except near the leading and trailing edges of the domain.

The first term on the right-hand side of (2.7) is a linear function of y, and is associated with the imposed pressure gradient $-\mathrm{d}(P_e/\rho)/\mathrm{d}x$ or $U_e\,\mathrm{d}U_e/\mathrm{d}x$. In an APG (FPG) TBL, the parameter a_I is positive (negative) due to the sign of $\mathrm{d}U_e/\mathrm{d}x$. Additionally, a_I can also be expressed as

$$a_I = -\frac{\delta_e}{|V_e|}\frac{\mathrm{d}U_e}{\mathrm{d}x} = \frac{\left.\dfrac{\partial V}{\partial y}\right|_e}{\dfrac{|V_e|}{\delta_e}}. \tag{3.1}$$

The parameter a_I can therefore be interpreted as the ratio of two slopes, namely the slope $\partial V/\partial y|_e$ of the mean wall-normal velocity profile at the boundary-layer edge, and the slope of $|V_e|/\delta_e$. This relationship is illustrated in figure 10, where the normalized mean wall-normal velocity V/V_e is plotted against the normalized wall-normal distance y/δ_e.

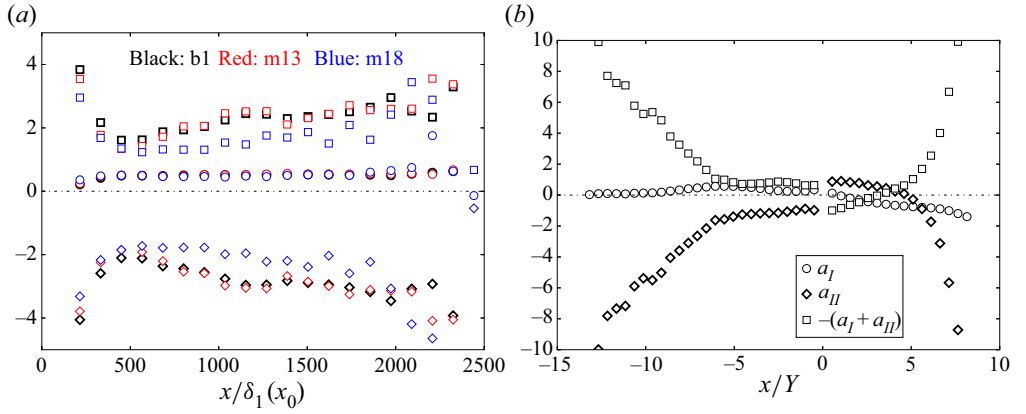

Figure 9. Pre-factors of the three terms on the right-hand side of (2.7). (*a*) Well-resolved LES of near-equilibrium APG TBL by Bobke *et al.* (2017). (*b*) The DNS of NEPG TBLs by Coleman *et al.* (2018). To prevent clutter, only every 100th grid in x is plotted.

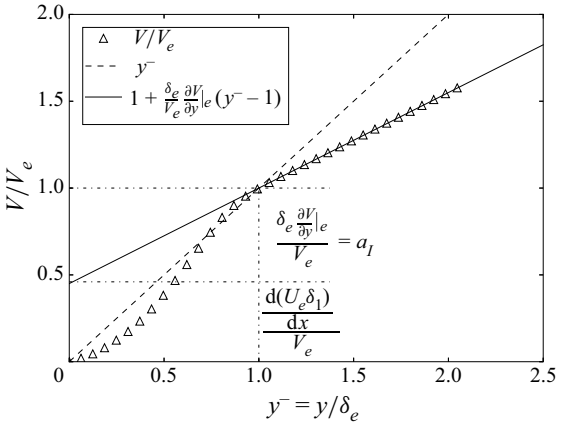

Figure 10. Visual representation of terms in (2.6) for $V/|V_e|$.

In the case of an APG TBL, where V_e is positive, this figure is equivalent to figure 6(*a*). On the other hand, in an FPG TBL where V_e is negative, figure 10 is analogous to vertically flipping figure 6(*b*) onto the positive side.

Figure 11 illustrates the impact of pressure gradient on the ratio of the two terms on the right-hand side of (2.6), as shown in figure 10. In the ZPG TBL, the ratio is zero since $\mathrm{d}U_e/\mathrm{d}x = 0$. In the near-equilibrium APG TBL, as observed in figure 11(*a*), the ratio remains nearly constant at 1. For the FPG TBL, both δ_e and δ_1 decrease in the x-direction, indicating a thinner boundary layer. In the non-equilibrium TBL simulated by Coleman *et al.* (2018), the product $U_e\delta_1$ initially decreases in the FPG TBL region and then increases towards the end of the simulation domain. Consequently, in the FPG region of the DNS data, the ratio can be either positive or negative, and its magnitude can exceed 1 significantly.

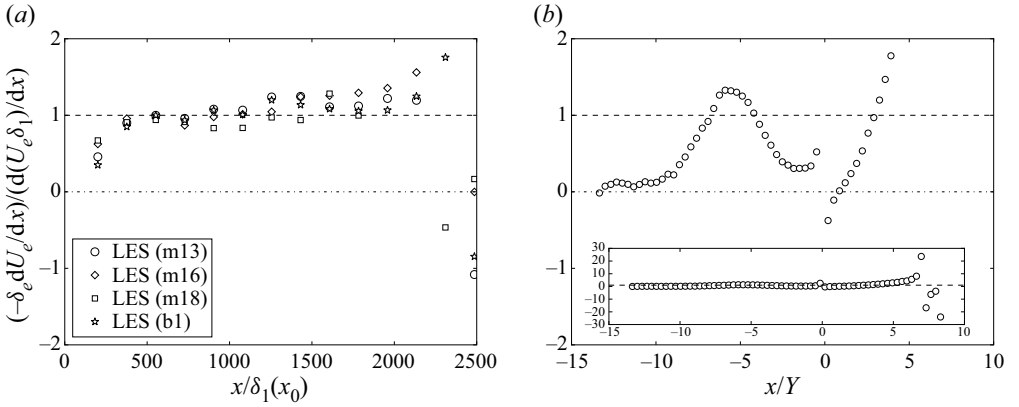

Figure 11. Ratio of the two terms on the right-hand side of (2.6). (*a*) Well-resolved LES of APG TBLs by Bobke *et al.* (2017). (*b*) The DNS of NEPG TBLs by Coleman *et al.* (2018).

The ratio between a_I and a_{II} is equivalent to the pressure gradient parameter Λ defined by Castillo & George (2001), with the only difference being a negative sign:

$$\frac{a_I}{a_{II}} = \frac{\delta_e \dfrac{\mathrm{d}U_e}{\mathrm{d}x}}{U_e \dfrac{\mathrm{d}\delta_e}{\mathrm{d}x}} = -\Lambda. \tag{3.2}$$

From their analysis of experimental data, Castillo & George (2001) reported that the pressure gradient parameter Λ is approximately 0.22 for APG TBLs, and -1.92 for FPG TBLs. However, the universality of these values has been a topic of debate, as pointed out by Maciel, Rossignol & Lemay (2006).

In near-equilibrium APG TBLs, the last term on the right-hand side of (2.5) is negligible. Additionally, as illustrated in figure 12, the ratio of $-\delta_e \,\mathrm{d}U_e/\mathrm{d}x$ to $(\delta_1/\delta_e)\,\mathrm{d}(U_e\delta_e)/\mathrm{d}x$ is approximately 1 within the region $1000 \lesssim x/\delta_1(x_0) \lesssim 2200$. Setting the ratio in figure 12 to be 1, the pressure gradient parameter defined by Castillo & George (2001) can be approximated as

$$\Lambda = -\frac{a_I}{a_{II}} = \frac{-\delta_e \dfrac{\mathrm{d}U_e}{\mathrm{d}x}}{U_e \dfrac{\mathrm{d}\delta_e}{\mathrm{d}x}} \approx \frac{1}{1+\dfrac{\delta_e}{\delta_1}} \quad \text{(near-equilibrium APG TBL)}. \tag{3.3}$$

Figure 13 compares the approximation (3.3) with experimental and LES data. While both the experimental and LES data show that Λ is not constant, they agree well with the predicted trend given by (3.3).

Figure 14(*a*) shows the ratio of the first two terms in (2.5) for V_e from the DNS data of NEPG TBLs by Coleman *et al.* (2018). The ratio is approximately 1 over a short distance within the APG region, and Λ is close to the value 0.22 suggested for the near-equilibrium APG TBLs, as shown in figure 14(*b*). However, it is important to note that Λ is not constant from the leading edge to the end of the APG region, but exhibits a smooth variation. As shown in figure 14(*b*), the approximation in (3.3) works well for estimating Λ in the APG TBL when it is in a near-equilibrium state. However, this approximation is not valid for FPG TBLs.

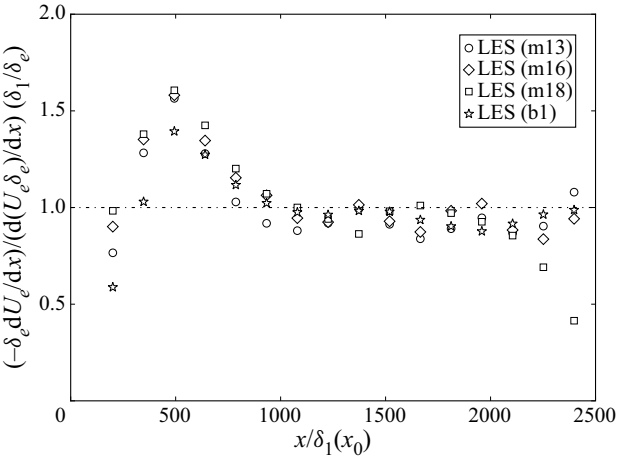

Figure 12. Ratio of $-\delta_e(\mathrm{d}U_e/\mathrm{d}x)$ to $(\mathrm{d}(U_e\delta_e)/\mathrm{d}x)(\delta_1/\delta_e)$. Data are from the well-resolved LES of near-equilibrium APG TBLs by Bobke *et al.* (2017).

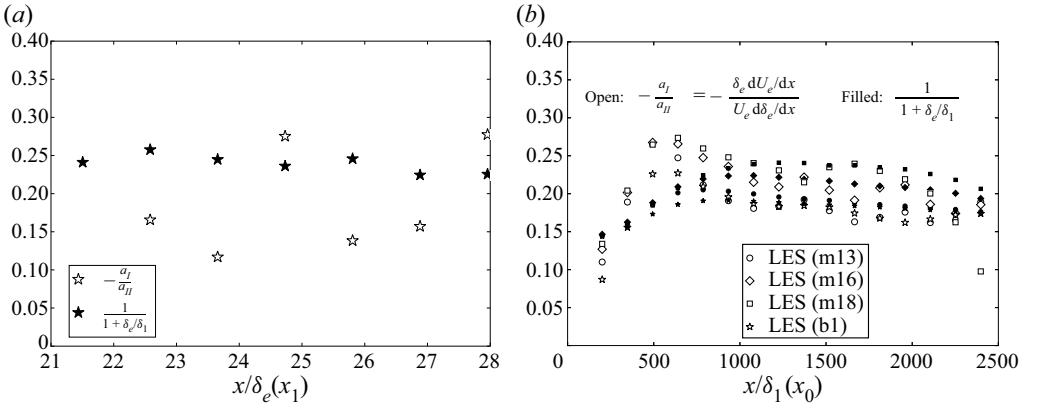

Figure 13. (*a*) Comparison of the approximate (3.3) and experimental data of Skåre & Krogstad (1994). The x-location is normalized by the boundary-layer thickness at the first measurement station. (*b*) Comparison of the approximate (3.3) and well-resolved LES data of near-equilibrium APG TBLs by Bobke *et al.* (2017).

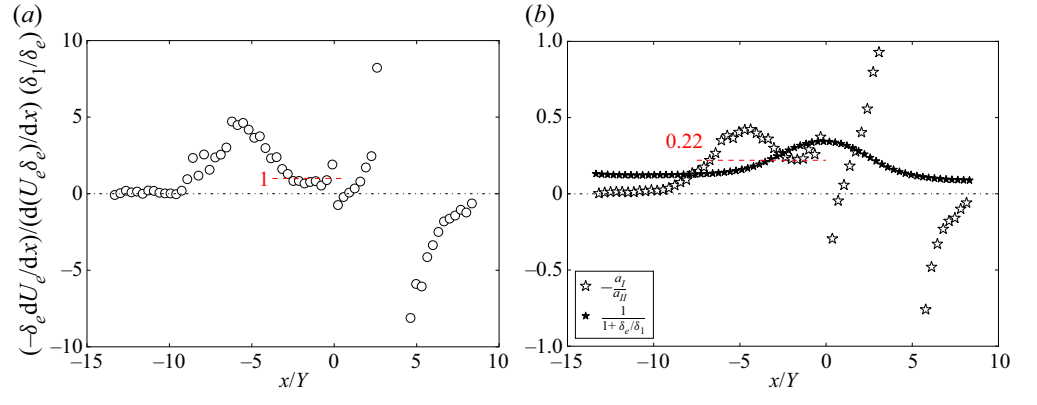

Figure 14. (*a*) Ratio of the first two terms on the right-hand side of (2.5) for V_e. (*b*) Plots of $\Lambda = -a_I/a_{II}$ and DNS data of NEPG TBLs by Coleman *et al.* (2018).

The variation of Λ in the region $0 \lesssim x/Y \lesssim 7$ is more complicated. For $0 \lesssim x/Y \lesssim 4$, where a strong FPG is present, U_e increases while δ_e decreases in the x-direction. As a result, a_I becomes negative, a_{II} becomes positive, and Λ becomes positive. However, at approximately $x/Y = 5$, $\mathrm{d}\delta_e/\mathrm{d}x \approx 0$ (see figure 1*b*), causing Λ to diverge to infinity. Beyond this point, i.e. for $x/Y \gtrsim 5$, δ_e begins to increase in the x-direction, despite the presence of a weak FPG. This results in a negative value of Λ.

The right-hand side of (3.3), computed from an integral quantity δ_1, provides greater numerical robustness and consistent values. It is close to the value suggested by Castillo & George (2001) for near-equilibrium flow conditions (figure 13*b*). Even in the non-equilibrium flow studied by Coleman *et al.* (2018), the approximation remains almost constant in the first part of the APG region sufficiently upstream of separation. In accordance with Wei & Knopp (2023), δ_1 corresponds to the wall distance y_m of maximum Reynolds shear stress. In flows approaching equilibrium, the position of y_m undergoes minimal changes.

4. Summary

This study investigates the behaviour of the mean wall-normal velocity in turbulent boundary layers (TBLs) subjected to pressure gradients. Through rigorous derivation, new analytical equations are developed to describe accurately the distribution of the mean wall-normal velocity and its value at the boundary-layer edge. These analytical equations are validated thoroughly against two independent numerical simulation datasets, demonstrating excellent agreement. Importantly, the evaluation of the simulation data highlights the robustness of the derived equations, confirming their independence from the specific method used to determine the boundary-layer edge.

The analytical equation for the mean wall-normal velocity is decomposed into four components, with only one of them involving the streamwise derivative of the U profile. In near-equilibrium TBLs, this component is found to be negligible, while in non-equilibrium cases, it plays a significant role. Furthermore, this study explores the characteristics of the pre-factors in the analytical equation for the mean wall-normal velocity, and establishes a close connection between the ratio of these pre-factors and a pressure-gradient parameter defined previously in the literature. By bridging an existing gap in the literature, this analysis enhances our understanding of the behaviour of TBLs under pressure gradients, contributing to more comprehensive knowledge in this field. Overall, this work represents a significant advancement in our knowledge of TBLs, and provides valuable insights for the analysis and prediction of mean wall-normal velocity profiles in such flows.

Acknowledgements. We would like to extend our sincere appreciation to Dr G. Coleman for generously sharing the DNS data with us, as well as for dedicating time to review our draft and providing us with valuable feedback.

Funding. T.K. would like to express his gratitude for the funding provided by the Deutsche Forschungsgemeinschaft (DFG) under the project 'Complex wake flows' (grant no. KN 888/3-2). R.V. acknowledges financial support from ERC grant no. 2021-CoG-101043998, DEEPCONTROL.

Declaration of interests. The authors report no conflict of interest.

Author ORCIDs.
Tie Wei https://orcid.org/0000-0001-7256-6052;
Zhaorui Li https://orcid.org/0000-0003-1858-2857;
Tobias Knopp https://orcid.org/0000-0002-3161-5353;
Ricardo Vinuesa https://orcid.org/0000-0001-6570-5499.

Appendix A. Determination of the boundary-layer edge

Accurately determining the location of the boundary-layer edge is essential for consistent analysis of boundary-layer flow data (see e.g. Vinuesa *et al.* 2016; Cantwell 2021; Subrahmanyam *et al.* 2022). In studies of boundary-layer flow over a flat plate, a widely adopted method involves utilizing the mean streamwise velocity profile to identify the boundary-layer edge. Specifically, the boundary-layer edge is determined as the position where the mean streamwise velocity reaches a certain percentage, typically 95 % or 99 %, of the free-stream velocity (see Young *et al.* 2007). The accuracy of this method relies on two factors: the spatial resolution of the measurements near the boundary-layer edge, and the constancy of the mean streamwise velocity outside the boundary layer.

Due to the gradual variation of mean streamwise velocity away from the wall, the measurements obtained in experimental studies often become sparse near the boundary-layer edge. The sparsity of data points near the boundary-layer edge poses a challenge in identifying the precise location of δ_e.

In numerical simulations, the spatial resolution is not a concern when employing the method based on the U profile. However, a potential challenge arises from the non-constancy of the mean streamwise velocity outside the TBL. Both experimental and numerical studies have revealed that the mean streamwise velocity U can exhibit wall-normal variations beyond the boundary-layer edge, particularly in TBLs experiencing strong pressure gradients (see e.g. Coleman *et al.* 2018). In such cases, it becomes unclear which velocity value should be used to determine the location of the boundary-layer edge based on the 95 % or 99 % criterion.

An alternative approach for determining the boundary-layer edge has been developed by Vinuesa *et al.* (2016), building upon the diagnostic plot concept introduced by Alfredsson, Segalini & Orlü (2011). This method involves plotting the ratio $u_{rms}/(U\sqrt{H_{12}})$ (where u_{rms} is the root-mean-square of the streamwise velocity fluctuation, U is the mean streamwise velocity, and H_{12} is the shape factor) against the ratio U/U_e. The diagnostic plot was introduced originally to evaluate experimental data quality. However, Vinuesa *et al.* (2016) expanded this concept to determine the boundary-layer thickness. They discovered that the position where $U/U_e = 0.99$ aligns approximately with $u_{rms}/(U\sqrt{H_{12}}) = 0.02$.

Recently, a novel method has been developed by Wei & Knopp (2023) to determine the edge of TBLs by utilizing the Reynolds shear stress profiles. In this approach, the location δ_e is defined as the point where the Reynolds shear stress decreases to 1 % or 5 %, depending on the spatial resolution, of the maximum value of the Reynolds shear stress. This innovative method offers a consistently reliable approach to identify accurately the boundary-layer edge, leveraging the distinct behaviour exhibited by the Reynolds shear stress.

In figures 15(*a–e*), we illustrate the boundary-layer edge determination using the approach proposed by Wei & Knopp (2023). This illustration is based on DNS data from Coleman *et al.* (2018) at five different x-stations. The horizontal axis represents the profiles of the mean streamwise velocity, mean wall-normal velocity, and Reynolds shear stress, all normalized by their maximum magnitude. The vertical axis represents the wall-normal location normalized by the computational domain height. The vertical dashed line indicates the value $0.01R_{uv}|_{max}$, while the horizontal dashed line represents the corresponding wall-normal location, signifying the position of δ_e.

Figures 15(*f–j*) zoom in on the U profile near the boundary-layer edge. The horizontal dashed line represents the location of δ_e determined by the position of $0.01R_{uv}|_{max}$. In cases where the pressure gradient is relatively small (ix = 1000 or 6100), the mean streamwise velocity outside the boundary layer remains nearly constant, as depicted in

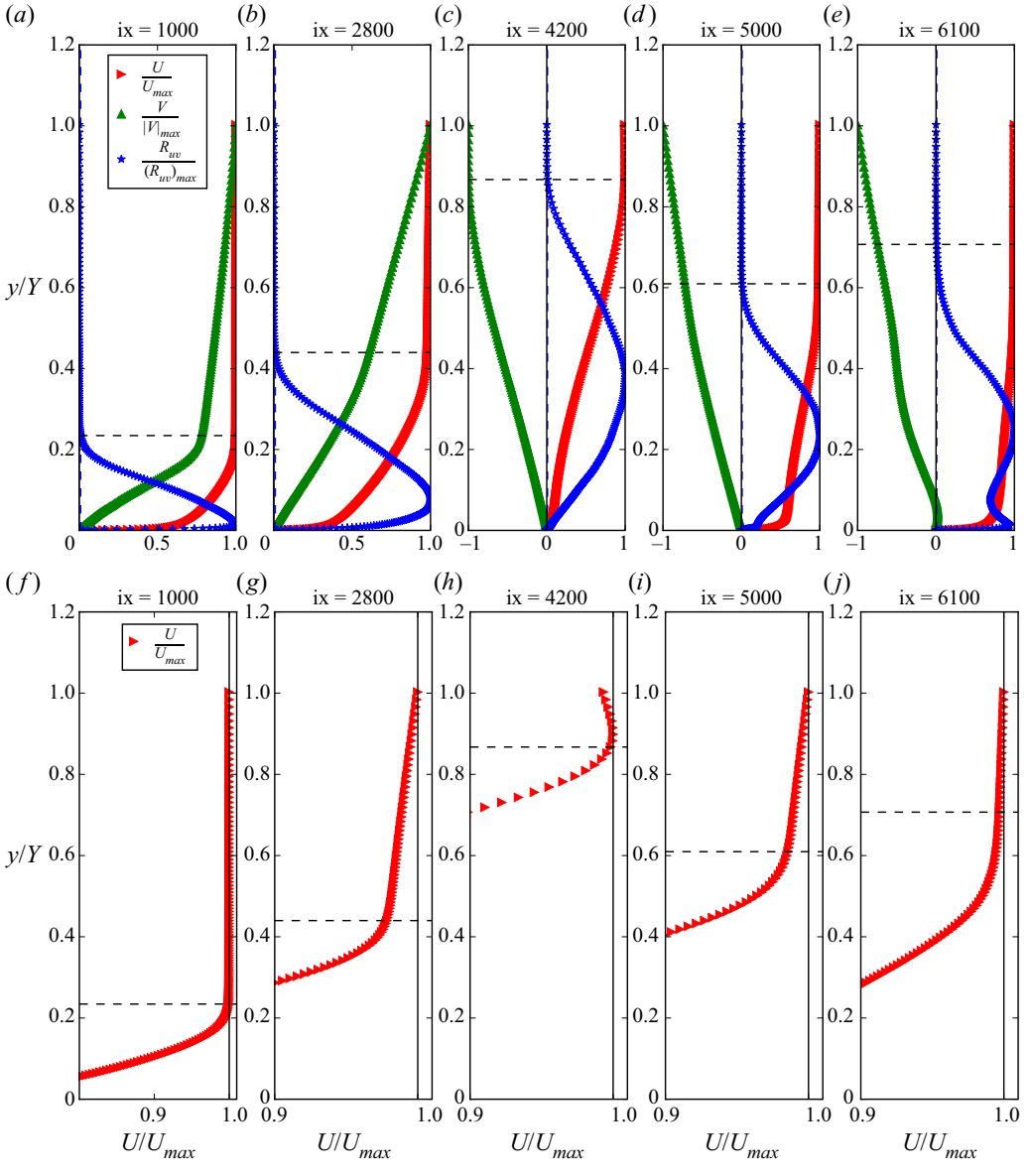

Figure 15. Boundary-layer edge determination using the $0.01R_{uv}|_{max}$ location. (*a–e*) Profiles of U, V and R_{uv}. (*f–j*) Profiles of U near the boundary-layer edge. These plots use DNS data of NEPG TBLs by Coleman *et al.* (2018).

figures 15(*f*) or 15(*j*). However, when subjected to significant adverse or favourable pressure gradients (ix = 2800, 4200, 5000), the mean streamwise velocity outside the boundary layer exhibits distinct variations with respect to the wall-normal distance. This variability poses a challenge in determining accurately the location of δ_e using the traditional 99 $\%U_e$ method.

Figure 16 compares δ_e determined via U profiles, R_{uv} profiles, and the diagnostic plot. Near the leading edge, where the streamwise velocity remains relatively constant outside the boundary layer, δ_e from $0.99U_{max}$ and the diagnostic plot method are

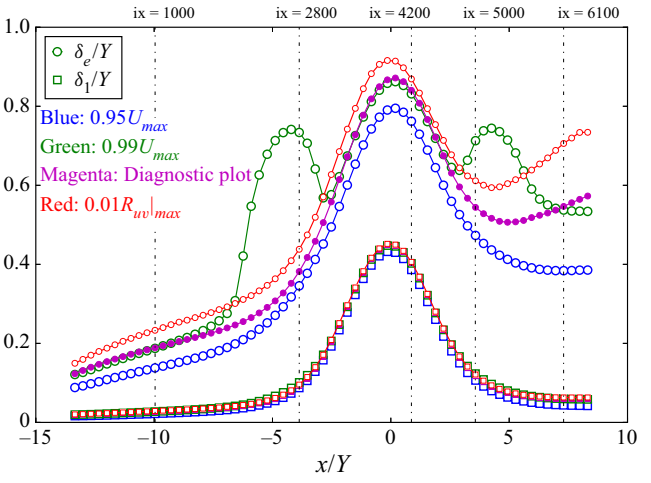

Figure 16. Comparison of δ_e determination using U profiles and R_{uv} profiles, with DNS data of NEPG TBLs by Coleman *et al.* (2018).

similar, in line with Vinuesa *et al.* (2016). However, the boundary-layer thickness from $0.01R_{uv}|_{max}$ locations is slightly larger, particularly near the domain outlet. Knopp *et al.* (2021) and Knopp (2022) observed that δ_{99} aligns closely with other methods used in the literature for determining boundary-layer thickness, such as the composite law-of-the-wall/law-of-the-wake by Coles & Hirst (1969) and the approach proposed by Coleman *et al.* (2018). However, noticeable differences can arise in determining the boundary-layer edge under strong pressure gradients, as indicated by the distinct values obtained from $0.99U_{max}$, $0.01R_{uv}|_{max}$ or the diagnostic plot. Despite the disparity in δ_e determined from U profiles, R_{uv} profiles and the diagnostic plot, the calculated displacements δ_1 are remarkably similar (as demonstrated in figure 16), suggesting that the contribution near the boundary-layer edge to the integral of the U deficit is negligible.

Appendix B. Influence of δ_e and U_e determination on (2.6) and (2.7)

The mathematical derivation of (2.6) and (2.7) does not impose any specific method for determining δ_e or U_e. To demonstrate the independence of analytical equations accuracy from the definition of boundary-layer edge, we compare results from four δ_e determination methods: $0.95U_{max}$, $0.99U_{max}$, $0.01R_{uv}|_{max}$ and the diagnostic plot. Figure 17 displays U_e and V_e values from the boundary-layer edge determined using the four methods. As expected, the U_e values determined from the $0.95U_{max}$ location are lower than those obtained from $0.99U_{max}$, $0.01R_{uv}|_{max}$ or the diagnostic plot. Under strong APG or FPG ($-7 < x/Y < -4$ or $4 < x/Y < 6$), the $0.99U_{max}$ locations are farther away from the wall compared to the $0.01R_{uv}|_{max}$ locations or the diagnostic plot (see figure 16), resulting in larger values for V_e as well.

The analytical equation (2.6) for V_e involves three flow variables: $\delta_e(x)$, $\delta_1(x)$ and $U_e(x)$. In figure 4(*b*), the validity of (2.6) is substantiated by data obtained from $0.01R_{uv}|_{max}$ locations. Figure 18 assesses the impact of various boundary-layer edge determination methods on the reliability of (2.6). In figures 18(*a–c*), the three flow variables in (2.6) are determined from locations of $0.95U_{max}$, $0.99U_{max}$ in the U profiles, and the diagnostic plot, respectively. All the plots exhibit excellent agreement between directly simulated V_e and the analytical equation (2.6), regardless of the boundary-layer edge

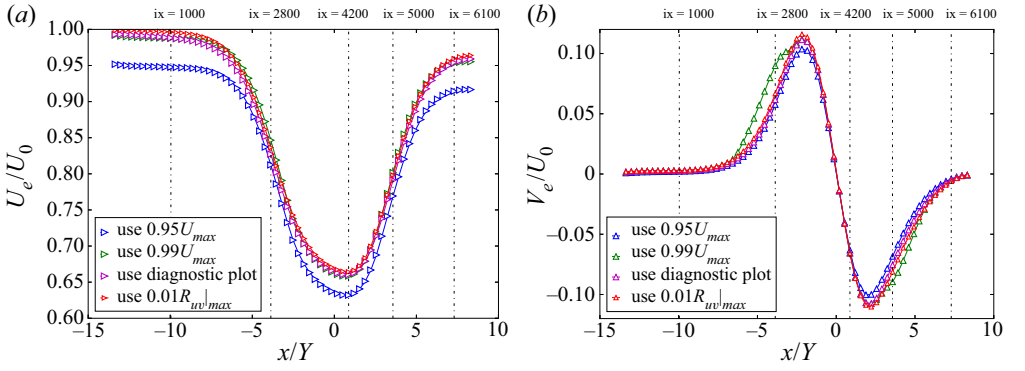

Figure 17. (*a*) Comparison of U_e determined at the locations of $0.95U_{max}$, $0.99U_{max}$, $0.01R_{uv}|_{max}$, and using the diagnostic plot. (*b*) Comparison of V_e using four boundary-layer edge determination methods. Plots use DNS data of NEPG TBLs by Coleman *et al.* (2018).

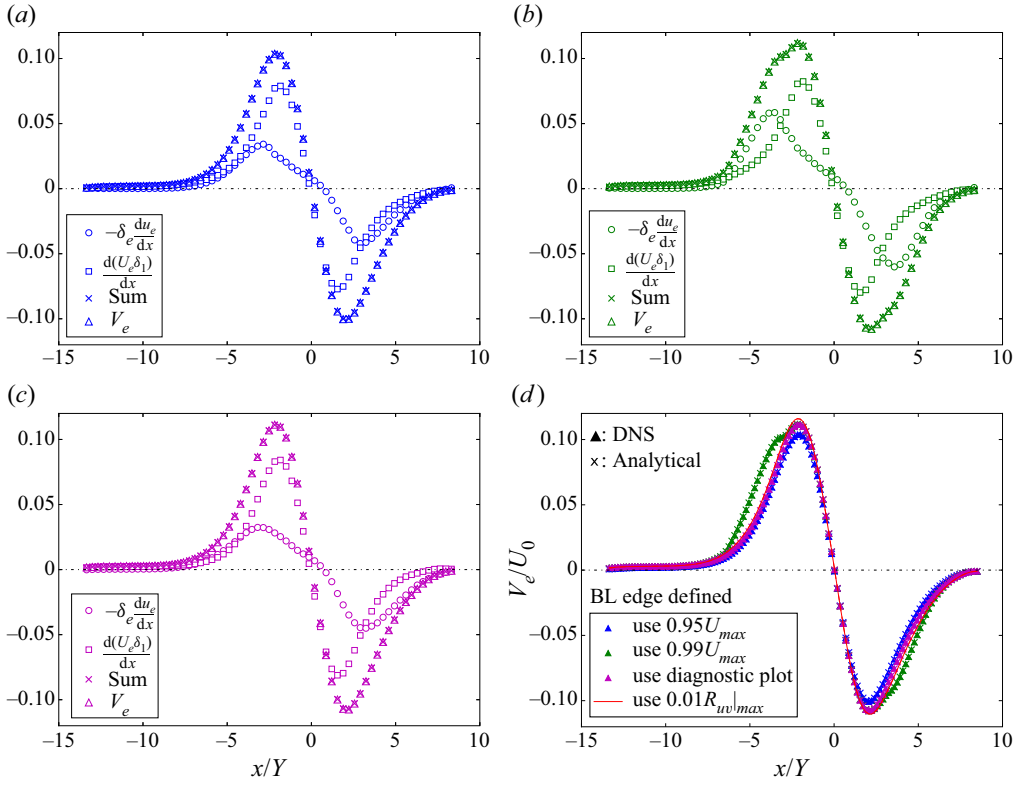

Figure 18. Comparing simulation data of V_e with analytical equation (2.6): (*a*) using $0.95U_{max}$ locations for V_e, U_e and δ_e; (*b*) using $0.99U_{max}$ locations for V_e, U_e and δ_e; (*c*) using the diagnostic plot for V_e, U_e and δ_e. (*d*) The DNS and analytical equation for V_e with different definitions of boundary-layer edge; DNS data from Coleman *et al.* (2018) for NEPG TBLs.

determination method. Figure 18(*d*) compares V_e simulated directly with V_e calculated analytically from (2.6), using four boundary-layer edge determination methods.

Figure 16 highlights distinct δ_e values arising from $0.95U_{max}$ and $0.99U_{max}$, particularly in regions of pronounced APG or FPG. Figure 19 displays mean wall-normal velocity

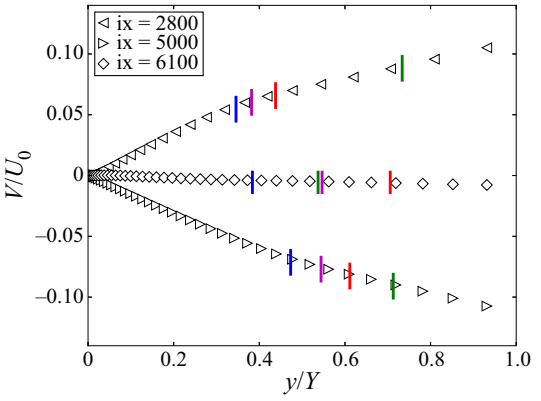

Figure 19. Mean wall-normal velocity profiles at three x-locations with corresponding boundary-layer edge markings: blue line indicates location of $0.95U_{max}$; green line indicates location of $0.99U_{max}$; magenta line indicates use of diagnostic plot; and red line indicates location of $0.01R_{uv}|_{max}$. Plots use DNS data of NEPG TBLs by Coleman *et al.* (2018).

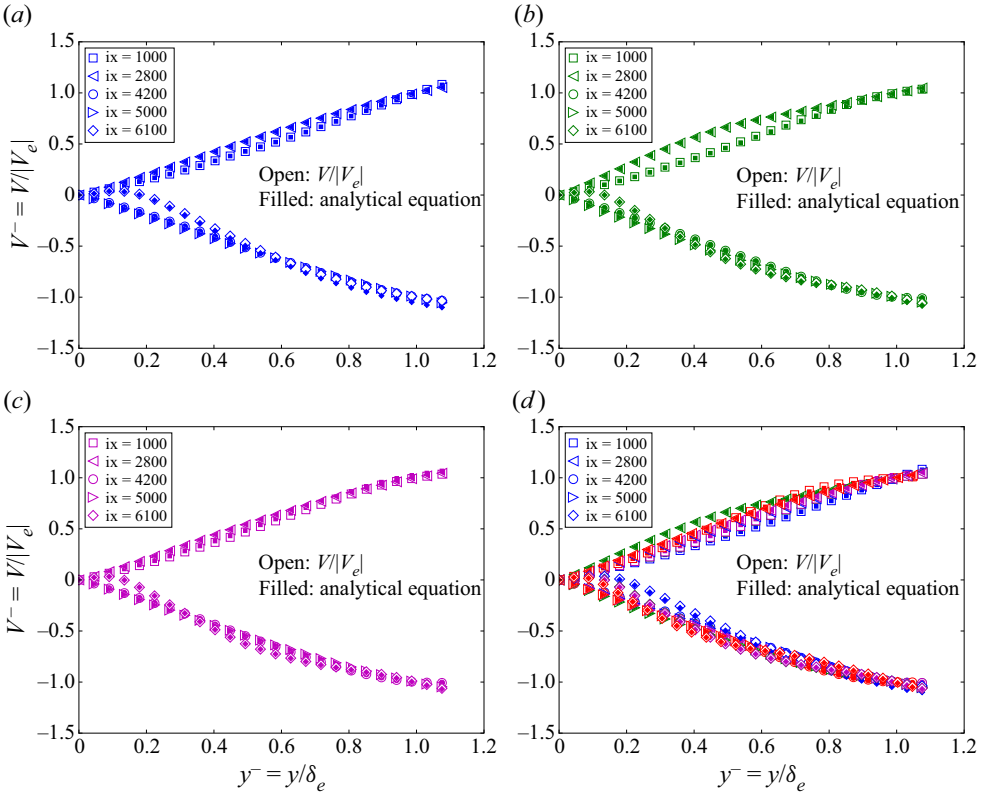

Figure 20. Normalized $V/|V_e|$ obtained directly from simulation data (open symbols) and the sum of terms on the right-hand side of (2.7) (filled symbols): (*a*) using $0.95U_{max}$ locations for δ_e; (*b*) using $0.99U_{max}$ locations for δ_e; (*c*) using the diagnostic plot for δ_e. (*d*) The DNS and analytical equation for V with different definitions of boundary-layer edge; DNS data of NEPG TBLs by Coleman *et al.* (2018).

at three x-locations (ix = 2800, 5000, 6100), illustrating differing δ_e values based on the four boundary-layer edge determination methods. At ix = 2800 (or $x/Y = -3.87$), for instance, δ_e from $0.99U_{max}$ is approximately 2.1 times that from $0.95U_{max}$, corresponding to a 1.5-fold higher V_e value. Although numerical δ_e values prove sensitive to boundary-layer-edge determination methods, U_e and δ_1 values exhibit less sensitivity due to the gradual outer region U variation, where its contribution to the velocity deficit integral within δ_1 is also minor.

In figure 7, the boundary-layer edge determined using $0.01R_{uv}|_{max}$ is employed to substantiate the validity of the analytical equation (2.7) for $V/|V_e|$. Figure 20 evaluates the reliability of (2.7) using four different definitions of boundary-layer edge. All the figures exhibit excellent agreement between the analytical results and directly simulated $V/|V_e|$ values. This compelling agreement provides strong evidence to affirm that the analytical equation (2.7) derived in this study is independent of the specific choice of the boundary-layer edge. Such independence underscores the robustness and reliability of the analytical equation.

While the analytical equation (2.7) remains valid regardless of the boundary-layer edge determination methods, the shapes of the $V/|V_e|$ versus y/δ_e profiles may differ as shown in figure 20. This discrepancy arises from the dependence of δ_e and V_e values on the chosen boundary-layer edge, as illustrated in figures 16 and 17(b). Consequently, the normalized $V/|V_e|$ profiles, plotted against y/δ_e, might display stretching or compression based on the selected δ_e and V_e, as evident in figure 20. Notably, figure 20(d) highlights that the profiles using δ_e determined through the approach proposed by Wei & Knopp (2023) and the diagnostic plot by Vinuesa *et al.* (2016) exhibit better collapse.

References

Alfredsson, P.H., Segalini, A. & Örlü, R. 2011 A new scaling for the streamwise turbulence intensity in wall-bounded turbulent flows and what it tells us about the 'outer' peak. *Phys. Fluids* **23** (4), 041702.

Bobke, A., Vinuesa, R., Örlü, R. & Schlatter, P. 2017 History effects and near equilibrium in adverse-pressure-gradient turbulent boundary layers. *J. Fluid Mech.* **820**, 667–692.

Cantwell, B.J. 2021 Integral measures of the zero pressure gradient boundary layer over the Reynolds number range $0 \leq Re_\tau < \infty$. *Phys. Fluids* **33** (8), 085108.

Castillo, L. & George, W.K. 2001 Similarity analysis for turbulent boundary layer with pressure gradient: outer flow. *AIAA J.* **39** (1), 41–47.

Clauser, F.H. 1954 Turbulent boundary layers in adverse pressure gradients. *J. Aeronaut. Sci.* **21**, 91–108.

Coleman, G.N., Rumsey, C.L. & Spalart, P.R. 2018 Numerical study of turbulent separation bubbles with varying pressure gradient and Reynolds number. *J. Fluid Mech.* **847**, 28–70.

Coles, D.E. & Hirst, E.A. 1969 *Computation of Turbulent Boundary Layers – 1968 AFOSR-IFP-Stanford Conference*. Thermosciences Division, Department of Mechanical Engineering, Stanford University.

Devenport, W.J. & Lowe, K.T. 2022 Equilibrium and non-equilibrium turbulent boundary layers. *Prog. Aerosp. Sci.* **131**, 100807.

Griffin, K.P., Fu, L. & Moin, P. 2021 General method for determining the boundary layer thickness in nonequilibrium flows. *Phys. Rev. Fluids* **6** (2), 024608.

Knopp, T. 2022 An empirical wall law for the mean velocity in an adverse pressure gradient for RANS turbulence modelling. *Flow Turbul. Combust.* **109**, 571–601.

Knopp, T., Reuther, N., Novara, M., Schanz, D., Schülein, E., Schröder, A. & Kähler, C.J. 2021 Experimental analysis of the log law at adverse pressure gradient. *J. Fluid Mech.* **918**, A17–1–A17–32.

Maciel, Y., Rossignol, K.-S. & Lemay, J. 2006 A study of a turbulent boundary layer in stalled-airfoil-type flow conditions. *Exp. Fluids* **41** (4), 573–590.

Mellor, G.L. 1966 The effects of pressure gradients on turbulent flow near a smooth wall. *J. Fluid Mech.* **24** (2), 255–274.

Mellor, G.L. & Gibson, D.M. 1966 Equilibrium turbulent boundary layers. *J. Fluid Mech.* **24** (2), 225–253.

MONTY, J.P., HARUN, Z. & MARUSIC, I. 2011 A parametric study of adverse pressure gradient turbulent boundary layers. *Intl J. Heat Fluid Flow* **32** (3), 575–585.

ROTTA, J. 1950 Über die Theorie turbulenter Grenzschichten. *Tech. Rep.* Mitteilungen aus dem Max-Planck-Institut für Strömungsforschung Nr. 1. (Translated as: On the theory of turbulent boundary layers. NACA Technical Memorandum no. 1344, 1953.).

SCHLICHTING, H. 1979 *Boundary-Layer Theory*. McGraw-Hill.

SKÅRE, P.E. & KROGSTAD, P.A. 1994 A turbulent equilibrium boundary layer near separation. *J. Fluid Mech.* **272**, 319–348.

SUBRAHMANYAM, M.A., CANTWELL, B.J. & ALONSO, J.J. 2022 A universal velocity profile for turbulent wall flows including adverse pressure gradient boundary layers. *J. Fluid Mech.* **933**, A16.

TENNEKES, H. & LUMLEY, J.L. 1972 *A First Course in Turbulence*. MIT Press.

TOWNSEND, A.A. 1956 *The Structure of Turbulent Shear Flow*. Cambridge University Press.

VINUESA, R., BOBKE, A., ÖRLÜ, R. & SCHLATTER, P. 2016 On determining characteristic length scales in pressure-gradient turbulent boundary layers. *Phys. Fluids* **28** (5), 055101.

VINUESA, R., NEGI, P., ATZORI, M., HANIFI, A., HENNINGSON, D.S. & SCHLATTER, P. 2018 Turbulent boundary layers around wing sections up to $Re_c = 1\,000\,000$. *Intl J. Heat Fluid Flow* **72**, 86–99.

WEI, T. & KLEWICKI, J. 2016 Scaling properties of the mean wall-normal velocity in zero-pressure-gradient boundary layers. *Phys. Rev. Fluids* **1** (8), 082401.

WEI, T. & KNOPP, T. 2023 Outer scaling of the mean momentum equation for turbulent boundary layers under adverse pressure gradient. *J. Fluid Mech.* **958**, A9.

WEI, T., LI, Z. & WANG, Y. 2023*a* New formulations for the mean wall-normal velocity and Reynolds shear stress in turbulent boundary layer under zero pressure gradient. *J. Fluid Mech.* **969**, A3:1–A3:15.

WEI, T., LIU, X., LI, Z. & LIVESCU, D. 2023*b* Planar turbulent wakes under pressure gradient: integral and self-similarity analyses. *Phys. Fluids* **35** (4), 045149.

YOUNG, D., MUNSON, B.R., OKISHI, T.H. & HUEBSCH, W. 2007 *A Brief Introduction to Fluid Mechanics*, 4th edn. Wiley.